Long-Term Colloidally Stable Aqueous Dispersions of ≤5 nm Spinel Ferrite Nanoparticles

Mirco Eckardt,[a] Sabrina L. J. Thomä,[a] Martin Dulle,[b] Gerald Hörner,[a] Birgit Weber,[a] Stefan Förster,[b] and Mirijam Zobel*[a]

Applications in biomedicine and ferrofluids, for instance, require long-term colloidally stable, concentrated aqueous dispersions of magnetic, biocompatible nanoparticles. Iron oxide and related spinel ferrite nanoparticles stabilized with organic molecules allow fine-tuning of magnetic properties via cation substitution and water-dispersibility. Here, we synthesize ≤ 5 nm iron oxide and spinel ferrite nanoparticles, capped with citrate, betaine and phosphocholine, in a one-pot strategy. We present a robust approach combining elemental (CHN) and thermal gravimetric analysis (TGA) to quantify the ratio of residual solvent molecules and organic stabilizers on the particle surface, being of particular accuracy for ligands with heteroatoms compared to the solvent. SAXS experiments demonstrate the long-term colloidal stability of our aqueous iron oxide and spinel ferrite nanoparticle dispersions for at least 3 months. By the use of SAXS we approved directly the colloidal stability of the nanoparticle dispersions for high concentrations up to 100 g L^{-1}.

1. Introduction

Iron oxide and related spinel ferrite nanoparticles, MFe_2O_4 (wherein M=Co^{2+} Fe^{2+}, Mg^{2+}, Ni^{2+}, Zn^{2+}), are of particular interest in various applications including biomedicine,[1–3] ferrofluids,[4–5] photocatalysis[6–7] or heterogeneous catalysis.[8–10] This interest arises because of their nano-size properties, which include finite size and surface effects, high saturation magnetization as well as superparamagnetism.[11] Further, these properties can readily be adjusted during the synthesis by altering the bivalent 3d metal cation,[12] providing a highly tunable, intensively studied material class.[12–16]

In recent years, much progress was made in the control of size and polydispersity of small iron oxide and spinel ferrite nanoparticles via various synthesis strategies, for instance coprecipitation[17] or microwave-assisted[7] approaches. The polyol route[18–20] for iron oxide and spinel ferrite nanoparticles has the advantage of high reaction temperatures >200 °C due to the high boiling point of the polyol solvents. High reaction temperatures lead to highly crystalline particles and hence high saturation magnetization (M_s).[21] The polyol solvent molecules further act as complexing agents for the 3d metal precursor species and nucleating particles, thus preventing particle aggregation during synthesis, resulting in very uniform particle sizes. It was postulated, that residual polyol molecules are still adsorbed after synthesis and purification to the nanoparticle surface, providing hydrophilicity, and hence water-dispersibility to e.g. cobalt ferrite nanoparticles,[22] or to iron oxide nanoparticles up to a concentration of 6 g L^{-1}.[23] Yet, both studies did neither experimentally address the colloidal stability of the nanoparticle dispersions, ruling out the presence of agglomerates, nor did they investigate particle growth over extended time periods during storage of the dispersions.

Despite the considerably high affinity of the polyol molecules to the ferrite nanoparticle surface, the interaction is weak enough for stronger capping agents to replace the polyols in order to enhance colloidal stability in aqueous dispersion or to tailor the surface functionalization for applications. Such a ligand-exchange can either be performed post-synthetic[22,24] or in a one-pot strategy.[19] In general, any desired functionality can be created, if the capping agent possesses a moiety with binding affinity to the nanoparticle surface, such as carboxyls, enediols[19,25] or phosphonic acids.[24,26] For iron oxide nanoparticles, Qu et al. identified various stabilizers, which in turn were accessible for further bioconjugation chemistry to load the nanoparticles with e.g. drugs, antibodies or cancer cells.[19] Shaikh et al. modified their ferrite nanoparticles such, that they direct reaction pathways in solvent-free catalysis.[25]

In ferrofluids and biomedical applications very high colloidal and long-term stability[11,27] of aqueous nanoparticle dispersions is required. Additionally, colloidal stability of magnetic nanoparticles even at high concentrations enables the adjustment of the magnetic response of such dispersions to a very high level.[5,22,28]

Despite ample literature on the synthesis and occasionally highlighted stability of ferrite nanoparticle dispersions, most

[a] M. Eckardt, S. L. J. Thomä, Dr. G. Hörner, Prof. B. Weber, Prof. M. Zobel
Department of Chemistry
University of Bayreuth
Universitätsstr.30
95440 Bayreuth (Germany)
E-mail: mirijam.zobel@uni-bayreuth.de
[b] Dr. M. Dulle, Prof. S. Förster
JCNS-1/IBI-8: Neutron Scattering and Biological Matter
Forschungszentrum Jülich Gmbh
Wilhelm-Johnen-Straße
52428 Jülich (Germany)

Supporting information for this article is available on the WWW under https://doi.org/10.1002/open.202000313

studies lack explicitly suitable techniques to monitor colloidal stability at high concentrations over extended time scales.[3,22–24,29–30] To our knowledge, those studies addressing colloidal stability, employ dynamic light scattering (DLS), which, usually, is performed on quite dilute nanoparticle dispersions, since the transmission would be too low for higher concentrations. For instance, cobalt ferrite nanoparticles were tailored for hyperthermia applications with phosphonic acid ligands. Their water-dispersibility up to one year was shown with DLS, yet the dispersion concentration was not specified.[24] The colloidal stability of polyanion-coated magnetite nanoparticles was investigated in dependence of pH and stabilizer concentration – though DLS measurements were only conducted at low concentrations of 0.1 $g\,L^{-1}$ without proof of long-term stability.[30] Polyethylene glycol (PEG)-functionalized magnetite particles formed stable colloidal dispersions at $c = 1.0\ g\,L^{-1}$ for temperatures up to 90 °C or storage times up to 4 months at room temperature (RT). This stability was reasoned by the irreversible binding of PEG derivatives with their catechol anchor groups to the magnetite surfaces with very high packing density.[3] Fan et al. stabilized iron oxide nanoparticles with a toxic viologene ligand to yield aqueous dispersions up to a concentration of 300 $g\,L^{-1}$.[29] Despite their application potential, i.e. the nanoparticles successfully isolated the protein avidin from solution with an efficiency of 96%, the colloidal stability was not addressed at all. From our point of view, the most suitable technique to confirm and monitor colloidal stability of concentrated dispersions, without the necessity for dilution as with DLS, is small angle X-ray scattering (SAXS).

Here we optimized a polyol synthesis strategy originally developed by Caruntu et al.,[18] to yield reproducibly, crystalline, superparamagnetic iron oxide and spinel ferrite (MFe_2O_4; M=Co^{2+}, Mg^{2+}, Ni^{2+}, Zn^{2+}) nanoparticles of 3–5 nm in diameter with low polydispersity. In particular, we established three different harmless and biocompatible ligands, namely citrate, betaine and phosphocholine, to stabilize aqueous colloidal dispersions in a concentration range of 5 to 100 $g\,L^{-1}$ over at least 3 months without significant particle growth and agglomeration in dispersion as evidenced by SAXS. A robust TGA-CHN-approach (thermogravimetric and elemental analytics) to quantitatively determine the ratio of residual solvent and organic ligand on the particle surface is presented and further supported by Fourier transform infrared (FT-IR) spectroscopy. We used a large toolbox of characterization techniques to thoroughly characterize the particle size distribution with transmission electron microscopy (TEM), DLS, SAXS and X-ray diffraction (XRD) with pair distribution function (PDF) analysis.

2. Results and Discussion

2.1. Nanoparticle Synthesis

Magnetic spinel ferrite nanoparticles (MFe_2O_4, with M=Co^{2+}, Fe^{2+}, Mg^{2+}, Ni^{2+}, Zn^{2+}) were synthesized in a one-pot strategy at elevated-temperature in basic diethylene glycol (DEG) solution, functionalized with bio-compatible organic ligand molecules and redispersed to yield stable dispersions (see Figure 1 and S1). For this, we have used a modified synthesis route originally developed by Caruntu et al.[18,23] and Qu et al.[19] We have realized that these publications on syntheses of iron oxide and spinel ferrite nanoparticles contain three slightly different synthesis strategies. The three protocols differ in the volumes and concentrations of the precursor ($MCl_2 \cdot nH_2O$ and 2 $FeCl_3 \cdot 6H_2O$ in DEG) and the NaOH solutions, as well as in the hold time at the aging temperature. For iron oxide nanoparticles in case (i) concentrations of 0.17 M precursor and 0.45 M NaOH were used with a hold time of one hour,[18] while in case (ii) the concentrations were 0.08 M and 0.45 M with a hold time of two hours.[19,23] In case of the spinel ferrite nanoparticles various different conditions were used depending on the applied metal.[18] Caruntu et al.[23] state that different concentrations of the reagents, as well as varying rates and times of heating have no significant impact on the nanoparticle size and shape of iron oxide nanoparticles with an average diameter of 5.7 ± 0.9 nm. On the contrary, since we have observed an impact of concentrations and heating onto the particle sizes, we adapted the synthesis and chose identical reaction conditions for all our iron oxide and spinel ferrite nanoparticles, which were concentrations of 0.17 M precursor, 0.22 M NaOH solution, a heating ramp of 130 $K\,h^{-1}$ and a hold time of one hour. These conditions resulted in our study in particle diameters of 3 to 5 nm depending on the bivalent metal. We functionalized the surface of the iron oxide and spinel ferrite nanoparticles with three different ligands, namely citrate, betaine and phosphocholine, via a ligand-exchange reaction after ageing the nanoparticles at high temperature.[19] The reproducibility of our synthesis was proven by DLS and TEM analysis, carried out for two separate synthesis, at least (Table 1).

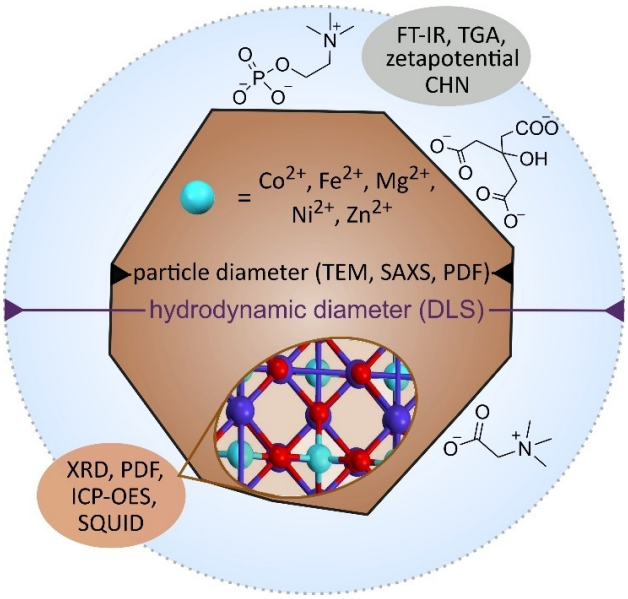

Figure 1. Illustrative scheme of a colloidally dispersed ferrite nanoparticle highlighting various characterization methods and their accessible insight.

Table 1. Particle sizes obtained from DLS, TEM, PDF and SAXS, as well as ζ-potential of ferrite and iron oxide nanoparticles with different organic stabilizing molecules. Fe:M ratio of ferrite nanoparticles was determined by ICP-OES. SAXS underpins the high colloidal stability of the dispersions and was performed on the same samples after ageing for 3 months. DLS diameter is based on number-weighted particle size distribution (converted from intensity distribution) and the PDI is calculated via cumulative frequency analysis. PDI values obtained from SAXS represent the lognormal particle size distribution. TEM and DLS particle diameters give the mean of at least two independent syntheses.

Nominal composition	stabilizer	d_{DLS} [nm] (PDI)	d_{TEM} [nm] (PDI)	d_{PDF} [nm]	d_{SAXS} [nm] (PDI) freshly prepared	after 3 months	ζ-potential [mV]	molar ratio (Fe: M) from ICP-OES
$CoFe_2O_4$	citrate	4.4 (0.2)	4.6 (0.2)	4.3	3.5 (0.3)[a]	3.6 (0.3)[a]	-49.1 ± 0.9	2.1
	betaine	4.1 (0.2)	3.8 (0.2)	4.3	3.5 (0.2)		46.7 ± 0.6	2.1
	phos	4.5 (0.2)	3.8 (0.2)	3.6	4.0 (0.2)		46.5 ± 1.1	2.0
$ZnFe_2O_4$	citrate	5.8 (0.2)	4.8 (0.2)	5.2	5.0 (0.2)	5.0 (0.2)	-45.9 ± 1.4	2.9
	betaine	5.1 (0.2)	4.4 (0.2)	4.7	3.6 (0.3)		38.4 ± 2.3	3.2
	phos	5.6 (0.3)	5.3 (0.2)	5.6	4.8 (0.2)		43.9 ± 1.8	2.9
$MgFe_2O_4$	citrate	4.7 (0.2)	3.6 (0.2)	3.5	2.8 (0.3)[b]	2.9 (0.3)[b]	-40.6 ± 1.9	2.0
	betaine	5.0 (0.2)	3.0 (0.2)	3.4	2.7 (0.3)		43.4 ± 1.2	2.7
	phos	5.6 (0.3)	3.6 (0.2)	3.2	3.5 (0.2)		27.6 ± 0.5	2.1
$NiFe_2O_4$	citrate	4.6 (0.2)	3.6 (0.3)	4.2	2.7 (0.6)		-34.5 ± 1.0	2.4
	betaine	5.8 (0.2)	4.5 (0.2)	4.9	3.8 (0.3)	3.3 (0.2)	34.4 ± 1.2	1.7
	phos	5.2 (0.2)	4.9 (0.2)	4.3	3.8 (0.3)		45.9 ± 1.0	2.0
Fe_3O_4	citrate	4.9 (0.3)	3.7 (0.2)	3.6	2.2 (0.4)	2.2 (0.4)	-36.0 ± 0.2	
	betaine	5.8 (0.3)	4.8 (0.2)	5.0	3.7 (0.3)	3.7 (0.4)	37.7 ± 0.3	
	phos	4.1 (0.3)	4.0 (0.2)	3.6	2.7 (0.3)	2.8 (0.3)	21.0 ± 0.8	

[a] minor second size fraction with diameters of 6.4 (0.5) nm for the fresh and 6.0 (0.5) nm for the older dispersion exists; [b] minor second size fraction with diameters of 5.7 (0.5) nm for the fresh and 5.5 (0.5) nm for the older dispersion exists.

2.2. Structure and Surface Characterization

Zeta potentials of all iron oxide and ferrite nanoparticle dispersions with either ligand are $|\zeta| > 20$ mV, indicating electrostatic stabilization. Citrate-stabilized particles show negative zeta potential due to free carboxylate groups pointing into the solvent.[31] Positive zeta potentials of phosphocholine- and betaine-stabilized samples reveal the surface-bound modification of the negatively charged phosphate and carboxyl groups, whereas the quaternary ammonium groups are directed into the water. Further, all incorporated stabilizers are biocompatible, enabling biomedical applications.

FT-IR measurements support ligand binding on the nanoparticle surface, see section 1.1 in the SI for data on citrate-functionalized ferrite as well as iron oxide nanoparticles.

Further, we quantified the amount of ligand species on the nanoparticle surfaces. Previously, elemental (CHN) analytics have not routinely been used to analyze the organic fraction in nanoparticle powders, and occasionally discrepancies in mass losses in TGA remain unresolved.[26] Indeed, a proper determination of surface-bound species is challenging, due to the possible co-existence of residual solvent from synthesis and organic ligand molecules for functionalization. It is very common to estimate surface coverages of ligand molecules on nanoparticle surface based on TGA data, without analyzing the organic decomposition products with further analytics like mass spectrometry. Alternatively, employed ligand masses during syntheses are mathematically converted to final ligand coverages,[19] although DEG and related polyols like triethylene glycol are known to remain on the nanoparticle surface despite purification[22,32] and part of the employed ligands frequently remain in solution.

Here, we show a robust approach by combining CHN and TGA analytics to quantify the ratio of remaining solvent molecules and all three employed stabilizers. This approach is in particular useful with high confidence for ligands containing heteroatoms, which are not present in the solvent and thus allow unique distinction between ligand and solvent in CHN (or if applicable CHNPS) analytics. Here, this holds for the nitrogen atoms in betaine and phosphocholine, which are not present in the DEG solvent. For the complete TGA and CHN analysis including calculation see section 1.2 of the SI. Further, the presence of DEG on the nanoparticle surface suggested by CHN analytics is also in accordance with FT-IR measurements (Figure S3). Since DEG cannot cause the measured zeta potentials under the redispersion conditions employed in our present study, here it is evidently the capping agents that provide the colloidal stability of our aqueous nanoparticle dispersions. The residual polyols might contribute sterically to the stabilization.

To determine the stoichiometry of M:Fe in our heteroatomic ferrites MFe_2O_4 ($M^{2+} \neq Fe^{2+}$), inductively coupled plasma optical emission spectrometry (ICP-OES) measurements have been performed (see section 3.1 in the SI). Only for $ZnFe_2O_4$ nanoparticles, minor deviations from the ideal stoichiometry are present.

The magnetic response of the dried citrate-stabilized iron oxide and spinel ferrite nanoparticles has been addressed by field-dependent SQUID magnetometry (see section 2 in the SI). Satisfactory fits to the Langevin equation could be obtained in all cases, yielding saturation magnetization which decreases along the series $Fe^{2+} \gg Co^{2+} > Zn^{2+} > Ni^{2+} > Mg^{2+}$. This order largely reflects the variation of the bulk saturation magnetization M_s(bulk), which scales negatively with decreasing particle dimensions.

XRD and PDF analysis confirm the high crystallinity of all ferrite and iron oxide nanoparticles, which results from the high temperatures maintained during synthesis. All ferrite XRD patterns can be indexed with the cubic spinel structure (see

section 3.2 in the SI). While XRD analyses crystal structures in reciprocal space, the PDF corresponds to a histogram of all interatomic distances in real space. Therefore, PDF is well suited to structurally characterize short-range order and nanomaterials in general. PDF refinements of the spinel ferrite nanoparticles based on the cubic spinel structure *Fd-3m* describe the experimental data well in a fit range of 1.7 to 50 Å. For a better description of the local structure up to 5 Å, a parameter (Occ_{oct}), which accounts for possible vacancies on the octahedral cation positions, has to be introduced (Figure S8 and Table S3).

According to Cooper et al., we refined PDFs of iron oxide nanoparticles with the tetragonal space group $P4_32_12$ (maghemite space group) and variable occupancy on the octahedral position to check the maghemite:magnetite phase ratio in the nanoparticles based on the intensity ratio of the 3.0 and 3.5 Å PDF peaks, since magnetite nanoparticles readily undergo oxidation (see section 3.3 in the SI).[16] Based on these PDF refinements, our ca. 4 nm sized citrate- and phosphocholine-stabilized particles consist of 100% maghemite, whereas the bigger ca. 5 nm sized betaine-stabilized particles consist of 73% maghemite and 27% magnetite. This can be illustrated by a core-shell model existing of a 3.2 nm magnetite core and a 0.9 nm maghemite shell.

2.3. Stability and Particle Size

In addition to crystalline domain size from PDF, we employed TEM, DLS and SAXS to determine the nanoparticle diameters, see Table 1. The diameters observed with the different techniques deviate slightly, due to their measurement principle. Size determination via XRD and PDF is volume-weighted and crystalline domain sizes are accessed. In contrast, TEM is equally sensitive to differently sized particles, i.e. a number-weighted distribution. Histograms of particle diameters from TEM are refined with lognormal size distributions assuming spherical particle shape and show increasing mean diameters for M=Mg^{2+}, Co^{2+}, Fe^{2+}, Ni^{2+} and Zn^{2+}, respectively (see Figure 2 and S13). Crystalline domain sizes determined by PDF agree well with TEM particle diameters, showing that our nanoparticles are entirely crystalline. DLS yields the hydrodynamic particle diameter including a bound hydration layer, hence resulting in slightly larger particle diameters than all other techniques (Figure 1). The SAXS signal is based on the X-ray scattering contrast of solvent and solid particle, describing the inorganic solid diameter. The scattered intensities of both, SAXS and DLS, go with r_{NP}^6 (r_{NP} = particle radius). Therefore, the existence of few larger particles or agglomerates strongly impacts the resulting raw data but not the retrieved number-weighted size distribution, making SAXS utmost suited to validate colloidal stability while directly determining particle size and shape at the same time. On the contrary, DLS particles sizes are only estimated by the particle motion and spherical shape assumption. Particle diameters retrieved from SAXS are significantly smaller than the ones from TEM, but indicate narrow particle size distributions with low polydispersity indices (PDI) (for SAXS curves of spinel ferrites see Figure S14). This deviation between TEM and SAXS stems from the spherical shape model used in SAXS data analysis. Yet, the shapes of our spinel ferrite particles are slightly non-spherical as can be seen in TEM images. Hence, the SAXS fits apply a higher polydispersity index in combination with a smaller average particle diameter. SAXS data of citrate-functionalized magnesium and cobalt ferrite nanoparticles show an additional intensity increase for $Q < 0.4\ nm^{-1}$. As outlined above the raw data is depending on r_{NP}^6, thus, this can be ascribed to a very small fraction of agglomerates. In conclusion, our spinel ferrite and iron oxide nanoparticles, stabilized by betaine, phosphocholine and citrate, show a narrow, almost monodisperse (defined as 5% standard deviation) size distribution as conclusively evidenced by all employed techniques for almost all samples.

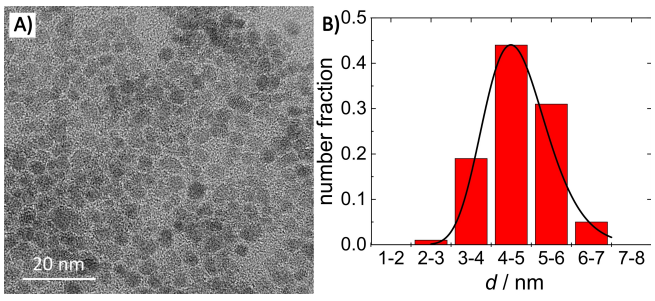

Figure 2. A) Representative TEM image of betaine stabilized zinc ferrite nanoparticles and B) the histogram of the size distribution with implemented lognormal fit.

As initially pointed out, applications require high colloidal stability of magnetic nanoparticles in aqueous dispersions at high concentrations over extended time periods. Figure 3 A shows the SAXS data of a freshly prepared dispersion of zinc ferrite nanoparticles with $5\ g\,L^{-1}$ measured five days after synthesis, and the same dispersion stored for 3 months and then measured. The particle diameters are unaltered, and not any agglomerates appear. Additionally, the colloidal stability up to 10 months in dispersion is confirmed by DLS measurements (Table S5). Moreover, SAXS allowed us to confirm the dispersion stability at higher concentrations of 50 and $100\ g\,L^{-1}$, as well as to determine particle sizes at these high concentrations. Due to the high density of the particles themselves even the highest concentrations investigated have volume fractions of $< 5\%$. For the fits no structure factor contributions were necessary. Multiple scattering for spherical particle dispersions shows itself by raising the apparent polydispersity with concentration. This we did not observe and thus can conclude that no significant amount of multiple scattering occurs. Figure 3 B shows exemplary SAXS data on 4 nm phosphocholine-stabilized cobalt ferrite particles with a PDI of 0.2 for concentrations of 5, 50 and $100\ g\,L^{-1}$ (for further data on iron oxides see Figure S15). Also for these high concentrations, the particle diameters do not change, and particles do not agglomerate, even when stored for 3 months as dispersions at RT. This highlights the outstanding stability of our aqueous dispersions.

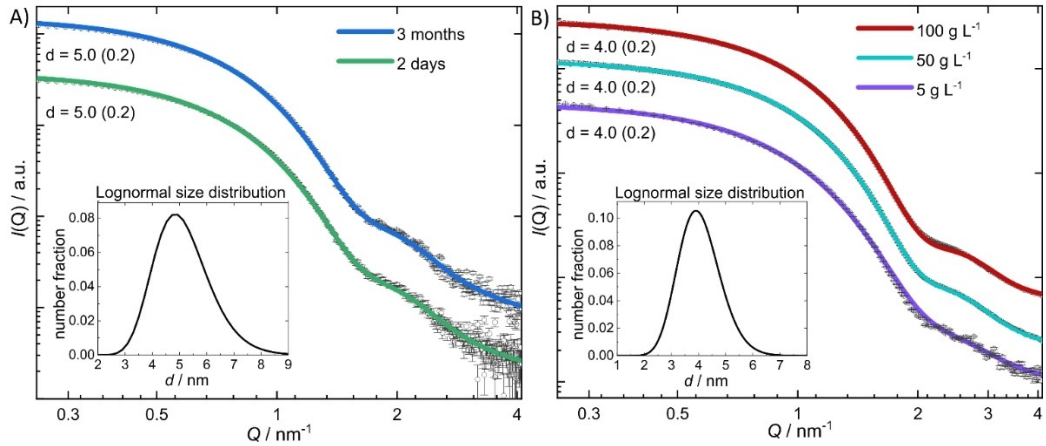

Figure 3. Experimental SAXS data and their fits. The dried nanoparticle powders were redispersed in water and measured within 7 days after redispersion. A) Aqueous dispersion of citrate-stabilized zinc ferrite nanoparticles (c = 5 g L^{-1}) 2 days after synthesis (green) and the same dispersion stored at RT for 3 months (blue). B) Aqueous dispersions of phosphocholine-stabilized cobalt ferrite nanoparticles at concentrations of 5 (purple), 50 (light blue) and 100 g L^{-1} (red) stored for 3.5 months. Curves are scaled for clarity. The insets show the appropriate lognormal size distribution.

3. Conclusions

The optimization of a simple and reproducible polyol method for the synthesis of crystalline iron oxide and spinel ferrite nanoparticles MFe_2O_4 (with M=Co^{2+} Fe^{2+}, Mg^{2+}, Ni^{2+}, Zn^{2+}) has been reported. The mean diameters of the monodisperse and entirely crystalline particles are 3–5 nm as evidenced by PDF, XRD, SAXS and DLS. Surface functionalization with citrate, betaine and phosphocholine achieves long-term and colloidally stable aqueous dispersions. Our robust TGA-CHN approach disentangles the fraction of organic solvent and ligand molecules on the particle surface, well in accordance with IR spectra. Aqueous dispersions were shown to be stable for nanoparticle concentrations up to 100 g L^{-1}, without significant particle growth or agglomeration for at least 3 months. All nanoparticle samples show superparamagnetic behavior in SQUID analysis, making them very interesting for applications, where highly stable and biocompatible magnetic nanoparticles are required at high concentrations, e.g. biomedicine or ferrofluids.

Experimental Section

Nanoparticle Synthesis

Chemicals for the nanoparticle synthesis were purchased and used without further purification: ethanol absolute (VWR), diethylene glycol (99%, Alfa Aesar), sodium hydroxide pellets (Merck), hydrochloric acid solution (in water 1 M, Grüssing GmbH), acetone and ethyl acetate (analytical grade, Fisher Scientific), cobalt(II) chloride hexahydrate (ACS reagent, ≥98%, Merck), nickel(II) chloride hexahydrate (≥98%, abcr), iron(II) chloride tetrahydrate (Glentham Life Sciences), magnesium hexahydrate (BioXtra, ≥98%), zink(II) chloride (puriss., ≥98%) and iron(III) chloride hexahydrate (puriss. p.a. reag., ≥99%, all Sigma Aldrich). Ligands for the nanoparticle surface modification were obtained as follows: phosphocholine chloride calcium salt tetrahydrate (98%) from abcr, betaine anhydrous (98%) from Alfa Aeasar and trisodium citrate dihydrate (99%) from Grüssing GmbH. Milli-Q water was used for the preparation of all dispersions.

Water-dispersible ferrite nanoparticles with diameters of 3 to 5 nm were obtained via hydrolysis of diethylene glycol (DEG) chelate complexes of Fe^{3+} and M^{2+} (M=Mg, Co, Ni, Fe or Zn) according to Caruntu et al.[18] $MCl_2 \cdot n\ H_2O$ (1 mmol) and $FeCl_3$ 6 H_2O (2 mmol) were dissolved in DEG (20 g). A solution of NaOH (8 mmol) in DEG (40 g) was added. The reaction solution was then degassed with argon for 2 hours and subsequently heated to 220 °C with a heating rate of 130 °C h^{-1}. The temperature was kept constant for 1 hour and then cooled to about 100 °C. At this point, a solution of 3 mmol capping agent dissolved in DEG/H_2O (3 mL) was added. After the addition of the ligand solutions, the nanoparticle dispersions in DEG were stirred for another hour while cooling to room temperature. The nanoparticle powder was precipitated by addition of acetone and isolated. For purification, the powder was washed with acetone and absolute ethanol three to five times and dried at room temperature. All nanoparticle powders were redispersible in water or HCl (50 mM) up to a concentration of 100 g L^{-1}.

Characterization

TEM measurements were performed with a JEOL JEM-2200FS field emission energy filtering transmission electron microscope (FE-EFTEM) operated at an acceleration voltage of 200 kV. Zero-loss filtered micrographs ($\Delta E \sim 0$ eV) were recorded with a bottom-mounted CMOS camera system (OneView, Gatan) and processed with DM 3.3 image processing software (Gatan). For each sample, 4 μL of very diluted nanoparticle dispersion were drop-casted on a carbon-coated meshed copper grid and dried in air. Particle sizes were obtained by counting 100 particles from at least three images.

Evaluation of the hydrodynamic diameters and zeta potential of the nanoparticles was performed with a Particle Analyzer Litesizer 500 (Anton Paar, Germany) at 25 °C in the automatic mode with a wavelength of 660 nm. The concentration of the nanoparticles was adapted so that the intensity was at least 300 kcounts sec^{-1}. Calculation of the number-weighted hydrodynamic radii was based on refractive indices and absorption coefficients from.[33] The zeta potential was calculated via the Smoluchowski approximation.

Small angle X-ray scattering (SAXS) patterns were recorded with the laboratory SAXS system "Ganesha-Air" from (SAXSLAB, Xenocs).

The X-ray source is a D2-MetalJet (Excillum) operating at 70 kV and 3.57 mA with Ga–K_α radiation ($\lambda = 0.1341$ nm) providing a very brilliant and a very small beam (< 100 μm). The beam was focused with a focal length of 55 cm using a specially made X-ray optic (Xenocs). Measurements were done in 2.1 mm borosilicate glass capillaries (Hilgenberg), code 1409364, Germany) at room temperature, and the transmitted intensity data were recorded by a position-sensitive detector (PILATUS 300 K, Dectris). To cover the range of scattering vectors between 0.026 and 3 nm^{-1}, different detector positions were used. The circularly averaged data were normalized to incident beam, sample thickness, and measurement time before subtraction of the solvent. All measurements were put on an absolute scale by standard-less absolute intensity calibration. Dispersions for SAXS measurements had typical concentrations of 5 $g\,L^{-1}$ and high concentration measurements were performed at 50 and 100 $g\,L^{-1}$. Fitting of the data was performed using SASView 4.2.2 and JScatter.[34] The fit range was $Q = 0.2$ to 5 nm^{-1}. Q is the wave vector transfer, calculated as $Q = 4\pi \sin(\theta)/\lambda$, with the wavelength λ and the scattering angle 2θ. A spherical hard sphere shape model was applied, except for the two citrate-stabilized magnesium and cobalt ferrite nanoparticle samples, where a bimodal size distribution (two spheres) was used. Scaling and background factor, particle radius and the polydispersity index of a lognormal size distribution were refined. Scattering length densities were set constant.

Powder X-ray diffraction (XRD) was carried out at room temperature with a STOE STADI P Mythen2 4 K diffractometer (Ge(111) monochromator; Ag $K\alpha_1$ radiation, $\lambda = 0.5594$ Å) using four Dectris MYTHEN2 R 1 K detectors in Debye-Scherrer geometry. Samples were measured in 0.5 mm diameter glass capillaries purchased from Hilgenberg (special purpose glass number 10) for 14 h. The Q-range was 20.4 $Å^{-1}$. For more information on this dedicated diffractometer for pair distribution function analysis, see.[35] PDF processing was carried out with xPDFsuite[36] using a Q_{max} of 13.0 to 17.5 $Å^{-1}$, and fitting was done with diffpy-CMI.[37] Parameters refined were the scale, cell parameters, crystallite size, correlated atomic motion, atomic position of oxygen, occupancy of octahedral sites and thermal parameters. Values for the degree of inversion of spinels were obtained from crystallographic information files and were fixed for the refinement.

Thermogravimetric analysis (TGA) measurements were performed from 30–1000 °C on a STA PT16000 (Linseis, Germany) with a heating ramp of 10 °C min^{-1} under argon atmosphere.

Elemental analysis of the nanoparticle powders was conducted with a Elementar vario EL III. 2 mg of dry nanoparticle powder was used per sample run.

Samples for ICP-OES were prepared by dissolving 0.1 $g\,L^{-1}$ of the synthesized nanoparticles in an aqueous solution of 37% HCl. The measurements were performed with a Varian Vista-Pro equipped with an ASX-510 autosampler.

Infrared spectra (IR) were collected with a JASCO FT/IR-6100 Fourier transform infrared (FT-IR) spectrometer with attenuated total reflectance (ATR) unit. Before the measurement, the instrument was flushed with nitrogen for 30 min. The spectra of an aliquot of dry nanoparticle powder were collected from 4000–400 cm^{-1} (0.25 cm^{-1} step size) and normalized to the transmittance at 4000 cm^{-1}.

Magnetic measurements were collected using a SQUID MPMS-XL5 instrument from Quantum Design. The field measurements at 300 K were performed in the hysteresis mode, in steps of 500 Oe from 100 Oe to 30 000 Oe and then down to −30 000 Oe. The samples were prepared in gelatin capsules held in a plastic straw. The raw data were corrected for the diamagnetism of the sample holder.

Acknowledgements

We acknowledge funding by the Deutsche Forschungsgemeinschaft (DFG, German Research Foundation) via SFB 840 (subprojects C7, B9 and A10) and a scholarship of the Young Academy of the Bavarian Academy of Sciences and Humanities. We thank Marco Schwarzmann for TEM and TGA support. We further thank the Bavarian Polymer Institute (BPI) for access to the keylabs 'Electron and Optical Microscopy'. We acknowledge Prof. M. Obst from BayCEER for ICP-OES, and Prof. S.J.L. Billinge and M. Grunert for diffpy-CMI support. This work benefited from the use of the SasView application, originally developed under NSF award DMR-0520547. SasView contains code developed with funding from the European Union's Horizon 2020 research and innovation program under the SINE2020 project, grant agreement No 654000.

Conflict of Interest

The authors declare no conflict of interest.

Keywords: colloidal stability · nanoparticles · spinel phase · SAXS · ferrites

[1] K. Zarschler, L. Rocks, N. Licciardello, L. Boselli, E. Polo, K. P. Garcia, L. De Cola, H. Stephan, K. A. Dawson, *Nanomedicine* **2016**, *12*, 1663–1701.
[2] N. Lee, D. Yoo, D. Ling, M. H. Cho, T. Hyeon, J. Cheon, *Chem. Rev.* **2015**, *115*, 10637–10689.
[3] E. Amstad, T. Gillich, I. Bilecka, M. Textor, E. Reimhult, *Nano Lett.* **2009**, *9*, 4042–4048.
[4] S. Kamali, M. Pouryazdan, M. Ghafari, M. Itou, M. Rahman, P. Stroeve, H. Hahn, Y. Sakurai, *J. Magn. Magn. Mater.* **2016**, *404*, 143–147.
[5] S. W. Charles, J. Popplewell in *Handbook of Ferromagnetic Materials, Vol. 2* (Ed.: E. P. Wohlfarth), Elsevier, North Holland, **1980**, pp. 509–559.
[6] E. Casbeer, V. K. Sharma, X.-Z. Li, *Sep. Purif. Technol.* **2012**, *87*, 1–14.
[7] K. Kirchberg, A. Becker, A. Bloesser, T. Weller, J. Timm, C. Suchomski, R. Marschall, *J. Phys. Chem. C* **2017**, *121*, 27126–27138.
[8] S. Anke, T. Falk, G. Bendt, I. Sinev, M. Hävecker, H. Antoni, I. Zegkinoglou, H. Jeon, A. Knop-Gericke, R. Schlögl, B. Roldan Cuenya, S. Schulz, M. Muhler, *J. Catal.* **2020**, *382*, 57–68.
[9] A. El Arrassi, Z. Liu, M. V. Evers, N. Blanc, G. Bendt, S. Saddeler, D. Tetzlaff, D. Pohl, C. Damm, S. Schulz, K. Tschulik, *J. Am. Chem. Soc.* **2019**, *141*, 9197–9201.
[10] H. Hajiyani, R. Pentcheva, *ACS Catal.* **2018**, *8*, 11773–11782.
[11] A. H. Lu, E. L. Salabas, F. Schuth, *Angew. Chem. Int. Ed. Engl.* **2007**, *46*, 1222–1244.
[12] A. L. Tiano, G. C. Papaefthymiou, C. S. Lewis, J. Han, C. Zhang, Q. Li, C. Shi, A. M. M. Abeykoon, S. J. L. Billinge, E. Stach, J. Thomas, K. Guerrero, P. Munayco, J. Munayco, R. B. Scorzelli, P. Burnham, A. J. Viescas, S. S. Wong, *Chem. Mater.* **2015**, *27*, 3572–3592.
[13] C. Nordhei, A. L. Ramstad, D. G. Nicholson, *Phys. Chem. Chem. Phys.* **2008**, *10*, 1053–1066.
[14] S. R. Cooper, L. K. Plummer, A. G. Cosby, P. Lenox, A. Jander, P. Dhagat, J. E. Hutchison, *Chem. Mater.* **2018**, *30*, 6053–6062.
[15] C. Pereira, A. M. Pereira, C. Fernandes, M. Rocha, R. Mendes, M. P. Fernández-García, A. Guedes, P. B. Tavares, J.-M. Grenèche, J. P. Araújo, C. Freire, *Chem. Mater.* **2012**, *24*, 1496–1504.
[16] S. R. Cooper, R. O. Candler, A. G. Cosby, D. W. Johnson, K. M. O. Jensen, J. E. Hutchison, *ACS Nano* **2020**, *14*, 5480–5490.
[17] T. Fried, G. Shemer, G. Markovich, *Adv. Mater.* **2001**, *13*, 1158–1161.
[18] D. Caruntu, Y. Remond, N. H. Chou, M.-J. Jin, G. Caruntu, J. He, G. Goloverda, C. O'Connor, V. Kolesnichenko, *Inorg. Chem.* **2002**, *41*, 6137–6146.
[19] H. Qu, D. Caruntu, H. Liu, C. J. O'Connor, *Langmuir* **2011**, *27*, 2271–2278.

[20] S. Ammar, N. Jouini, F. Fiévet, O. Stephan, C. Marhic, M. Richard, F. Villain, C. Cartier dit Moulin, S. Brice, P. Sainctavit, *J. Non-Cryst. Solids* **2004**, *345–346*, 658–662.
[21] V. Kumar, A. Rana, M. S. Yadav, R. P. Pant, *J. Magn. Magn. Mater.* **2008**, *320*, 1729–1734.
[22] M. Vasilakaki, N. Ntallis, N. Yaacoub, G. Muscas, D. Peddis, K. N. Trohidou, *Nanoscale* **2018**, *10*, 21244–21253.
[23] D. Caruntu, G. Caruntu, Y. Chen, C. J. O'Connor, G. Goloverda, V. L. Kolesnichenko, *Chem. Mater.* **2004**, *16*, 5527–5534.
[24] G. Baldi, D. Bonacchi, M. C. Franchini, D. Gentili, G. Lorenzi, A. Ricci, C. Ravagli, *Langmuir* **2007**, *23*, 4026–4028.
[25] M. Shaikh, M. Sahu, K. K. Atyam, K. V. S. Ranganath, *RSC Adv.* **2016**, *6*, 76795–76801.
[26] S. Mohapatra, P. Pramanik, *Colloids Surf. A* **2009**, *339*, 35–42.
[27] E. Amstad, M. Textor, E. Reimhult, *Nanoscale* **2011**, *3*, 2819–2843.
[28] D. Cabrera, J. Camarero, D. Ortega, F. J. Teran, *J. Nanopart. Res.* **2015**, *17*, 121.
[29] J. Fan, J. Lu, R. Xu, R. Jiang, Y. Gao, *J. Colloid Interface Sci.* **2003**, *266*, 215–218.
[30] A. Hajdú, E. Illés, E. Tombácz, I. Borbáth, *Colloids Surf. A* **2009**, *347*, 104–108.
[31] T. Milek, D. Zahn, *Z. Anorg. Allg. Chem.* **2016**, *642*, 902–905.
[32] M. Günay, H. Erdemi, A. Baykal, H. Sözeri, M. S. Toprak, *Mater. Res. Bull.* **2013**, *48*, 1057–1064.
[33] M. Polyanskiy, *Refractive index database* **2020**, *www.refractiveindex.info/*.
[34] R. Biehl, *PLoS One* **2019**, *14*, e0218789.
[35] S. L. J. Thomae, N. Prinz, T. Hartmann, M. Teck, S. Correll, M. Zobel, *Rev. Sci. Instrum.* **2019**, *90*, 043905.
[36] X. Yang, C. L. Farrow, P. Juhas, S. J. L. Billinge, *J. Appl. Crystallogr.* **2014**, arXiv:1402.3163 [cond-mat.mtrl-sci].
[37] P. Juhas, C. L. Farrow, X. Yang, K. R. Knox, S. J. Billinge, *Acta Crystallogr. Sect. A* **2015**, *71*, 562–568.

Manuscript received: October 23, 2020
Revised manuscript received: October 30, 2020